JOURNAL OF MATERIALS SCIENCE 26 (1991) 2833–2840

Borides in microcrystalline Fe–Cr–Mo–B–Si alloys

LIN YIJIAN, HU JIAN
Shanghai Iron and Steel Research Institute, 1001 Tai-Ho Road, Shanghai 200940, People's Republic of China

The formation and transformation of borides during melt-quenching and subsequent annealing in Fe–Cr–Mo–B–Si microcrystalline alloys was systematically investigated. Metastable M_3B forms during melt-quenching and soon disappears when annealing is carried out. During annealing, M_2B and M_3B_2 precipitate from the supersaturated α-Fe solid solution. As the annealing temperature is raised, M_2B gradually transforms from an Fe_2B-dominated state to a Cr_2B-dominated state, the remaining Fe_2B coexisting with Cr_2B in the form of stacking faults; meanwhile, there is a gradual increase in the Mo concentration in M_3B_2, together with the continuous increase in the lattice parameters of M_3B_2. The pre-formed M_2B and M_3B_2 further transform into $M_{23}B_6$ within a narrow temperature range around 925 °C.

1. Introduction

Commonly used as a microalloying element, boron is much less important than carbon in steels, and because of this, compared with carbides, the knowledge of borides in Fe-base alloys is still very meager to date. In recent years, new Fe-base microcrystalline alloys in which B is added as the dominant metalloid element have been developed [1]. The properties of these alloys depend on the kind, as well as the quantity and dispersity, of contained borides in these alloys. In the present work the formation and transformation of borides was systematically studied during rapid solidification and subsequent annealing in a typical Fe-base microcrystalline alloy, of composition $Fe_{70}Cr_{18}Mo_2B_9Si_1$ (at %).

2. Experimental procedure

The alloy was prepared by arc-melting, and subsequently melt-quenching into ribbons about 0.03 mm thick by the single-roller method in either air or vacuum. The ribbons were annealed in vacuum at different temperatures (300–1150 °C). Transmission electron microscopy (TEM) and scanning electron microscopy (SEM) were used to observe the structure of the as-melt-quenched and the annealed ribbons; X-ray diffraction (XRD) was used to analyse the phases as well as the changes in their lattice parameters and volume fractions; scanning transmission electron microscope energy dispersive spectra (STEMEDS) and electron probe microanalysis (EPMA) were used to determine the composition of the phases. In addition, the transformation temperatures of the borides were investigated by differential thermal analysis (DTA).

In order to establish the influence of B concentration on the borides, a series of $Fe_{79-x}Cr_{18}Mo_2Si_1B_x$ alloy with x varying from 4–20 at % was also investigated. These alloys were processed and analysed in the same way as above.

3. Results and discussion

3.1. As-melt-quenched structure

XRD analysis of the as-air-quenched $Fe_{70}Cr_{18}Mo_2Si_1B_9$ ribbons revealed that the structure was crystalline, it consisted of α-Fe and orthorhombic Fe_3B (o-Fe_3B). (Note: owing to their complex composition, virtually all the phases encountered in this work were multicomponent solid solutions, but for conciseness they are simply written here in the form of their base phase.) After the roller-side surface of the ribbons had been slightly polished (removing a layer ~ 1–2 μm thick) and appropriately etched, typical cellular solidification morphology was shown by SEM (Fig. 1a). By using TEM and selected-area diffraction (SAD), it was found that this cellular structure was composed of an α-Fe core (~ 0.3–0.5 μm diameter) and an (α-Fe + o-Fe_3B) eutectic which existed between the α-Fe cores. In transmission electron micrographs, this eutectic shows as a feather-like structure which extends from the α-Fe core boundary and is subdivided by black–white alternating streaks (Fig. 1b). According to the empirical formula between cell diameter (d, μm) and the cooling rate ($\dot{T}$, K s^{-1}), $d = 60\,\dot{T}^{-0.41}$ [2], the cooling rate during the melt-quenching of present alloys can be estimated to be of the order of 10^5 K s^{-1}. The above work illustrates that this cooling rate is not sufficient to suppress the segregation of B. During solidification, B was expelled from the α-Fe core into the regions between α-Fe cores, hence these regions became a B-enriched liquid phase of a lower melting point. In the later stage of the solidification, these regions transformed into (α-Fe + o-Fe_3B) eutectic.

0022–2461/91 $03.00 + .12

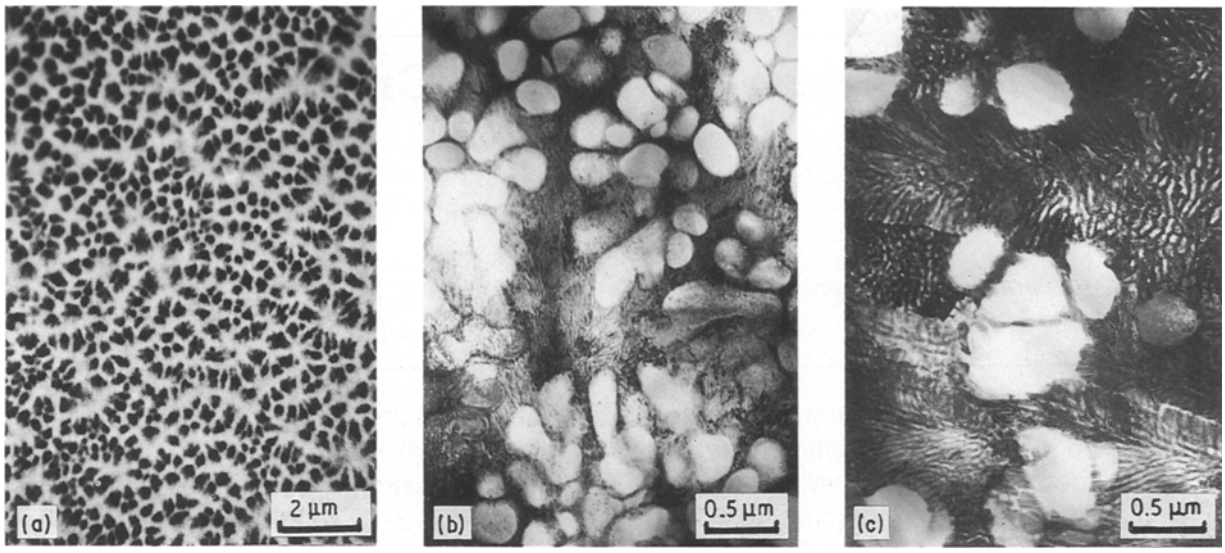

Figure 1 The microstructure of as-air-quenched ribbons: (a) scanning electron micrograph of cellular solidification structure; (b) transmission electron micrograph of α-Fe cell and (α-Fe + o-Fe_3B) eutectic between α-Fe cells; (c) transmission electron micrograph of well-developed eutectic.

Some regions were also found, which might be further from the roller-contact surface and have lower cooling rate, where the eutectic structure was perfectly developed (Fig. 1c). Owing to relatively better cooling condition, the ribbons melt-quenched in vacuum usually have an amorphous structure [3]. With increased B concentration, the glass-forming ability of the ribbons melt-quenched in air also increases and a completely amorphous structure was obtained in these ribbons when the boron percentage increased to 14 and 17 at% [4]. On the other hand, in contrast to Fe–B binary alloys, if the boron percentage reached 20 at%, the glass-forming ability of the present alloy dropped below a critical point. In this case, although the cooling conditions were unchanged, a completely crystalline structure was found once again. XRD analysis performed on these ribbons illustrated that apart from α-Fe lines, other diffraction lines were approximately in accordance with those of Cr_2B (F d d d, $a = 1.457$ nm, $b = 0.732$ nm, $c = 0.422$ nm) [5]. TEM observation showed that the crystalline structure in this case was a kind of (α-Fe + boride) eutectic (Fig. 2a). By using SAD, the boride was determined to have a hexagonal crystal lattice with $a = 0.422$ nm (Fig. 2b). This lattice can also be taken as a base-centred orthorhombic lattice with $a = 0.731$ nm and $b = 0.422$ nm and it is very close to the crystal lattice of Cr_2B. Hence it can be deduced that this boride is a metastable phase formed under rapid solidification conditions and very similar in crystal structure to Cr_2B. It is claimed [6] that Cr_2B is isomorphous in crystal structure with Mn_4B; sometimes it can have as much as 50% of the B-sites empty and thus becomes virtually Cr_4B. In the present work, if the boron concentration increases to 20%, the composition of the alloy will be just M_4B; this can be a favourable composition for the nucleation of this metastable boride and hence cause the abrupt decrease in the glass-forming ability.

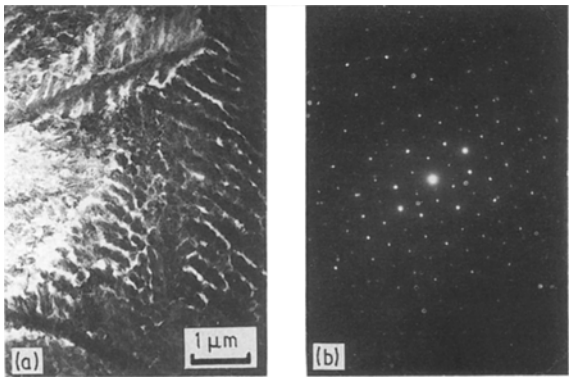

Figure 2 The as-quenched (metastable Cr_2B + α-Fe) eutectic in 20% B ribbons: (a) morphology of the eutectic; (b) SAD pattern of the metastable Cr_2B.

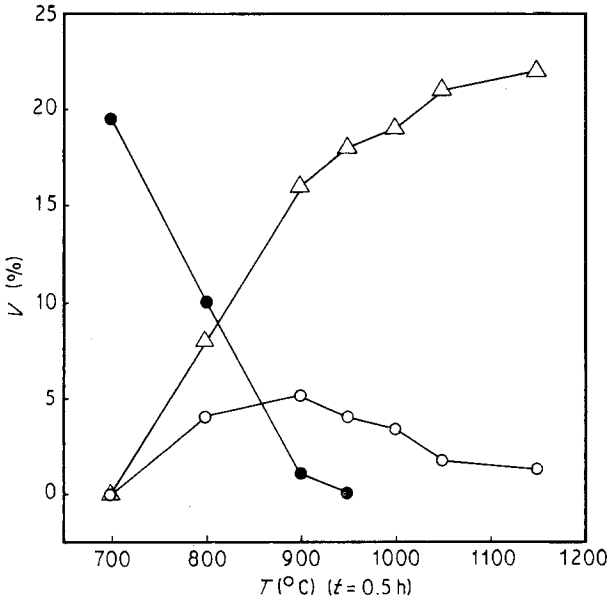

Figure 3 The relation between the volume fractions of borides and the annealing temperature. (△) Cr_2B, (○) M_3B_2, (●) Fe_2B.

3.2. Annealed structure

3.2.1. Boride at different annealing temperatures (300–1150 °C/0.5 h)

Detected by XRD, o-Fe_3B was found to disappear rapidly during annealing. Except that a few weak o-Fe_3B diffraction lines were still found in the XRD analysis of the ribbons annealed at 300 °C, the only boride which was found in the ribbons annealed in the temperature range from 300–700 °C was Fe_2B. Above 700 °C, as the annealing temperature was raised, the amount of Fe_2B decreased rapidly and became undetectable by XRD after annealing at or above 950 °C; instead, M_3B_2 and Cr_2B were formed. The amount of M_3B_2 increased to a peak at about 800–900 °C and then decreased, but Cr_2B showed a monotonic increase as the temperature was raised. Fig. 3 shows the change of volume fractions of the above borides after annealing at temperature above 700 °C.

Transmission electron micrographs (Fig. 4) show that the eutectic structure between the original cells has almost disappeared after annealing at 300 °C, but its outline still remained. Within the cells, a large

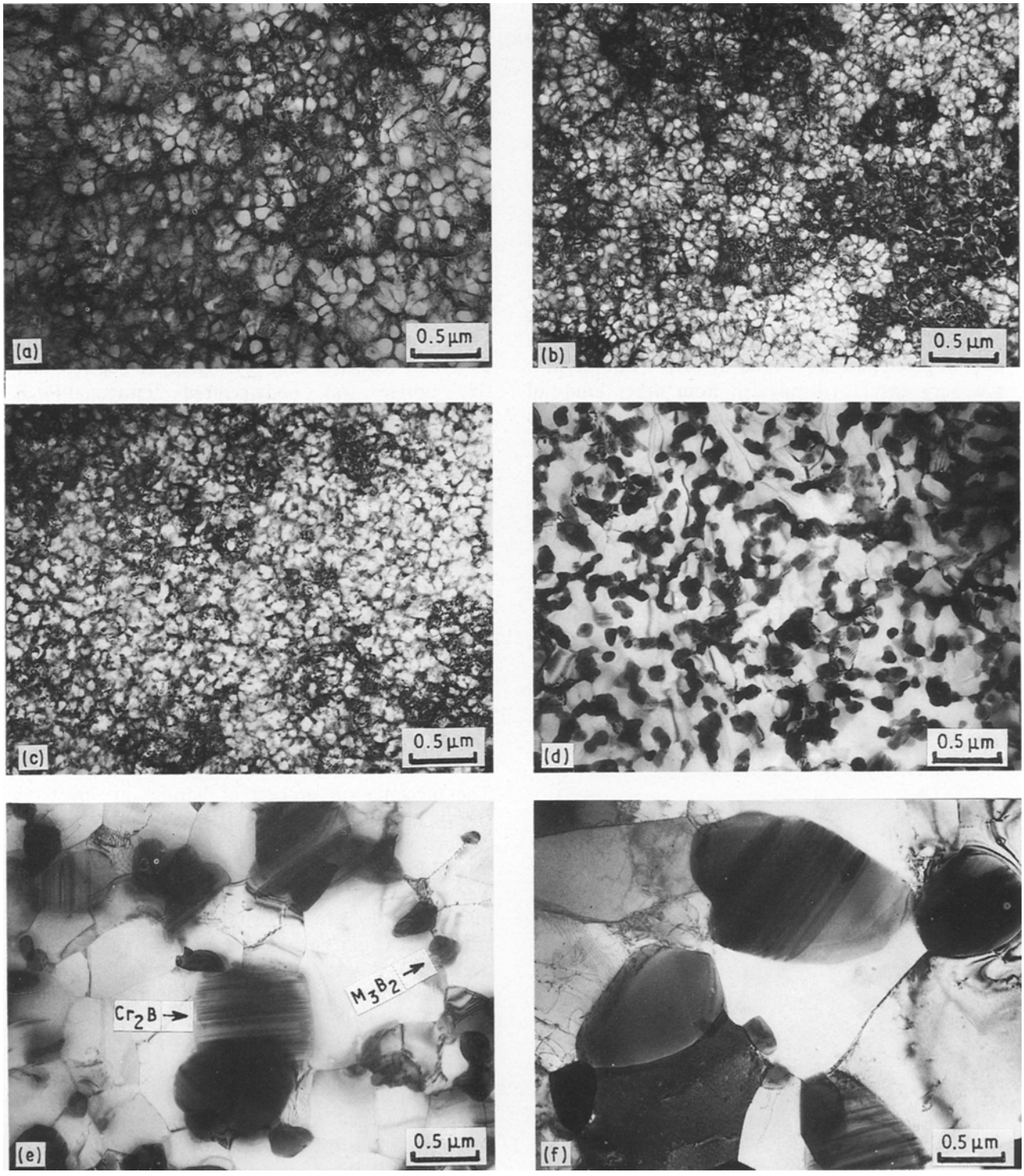

Figure 4 Transmission electron micrographs of the structures in ribbons annealed for 0.5 h at different temperatures: (a) 300 °C; (b) 500 °C, (c) 700 °C; (d) 800 °C; (e) 900 °C; (f) 1000 °C.

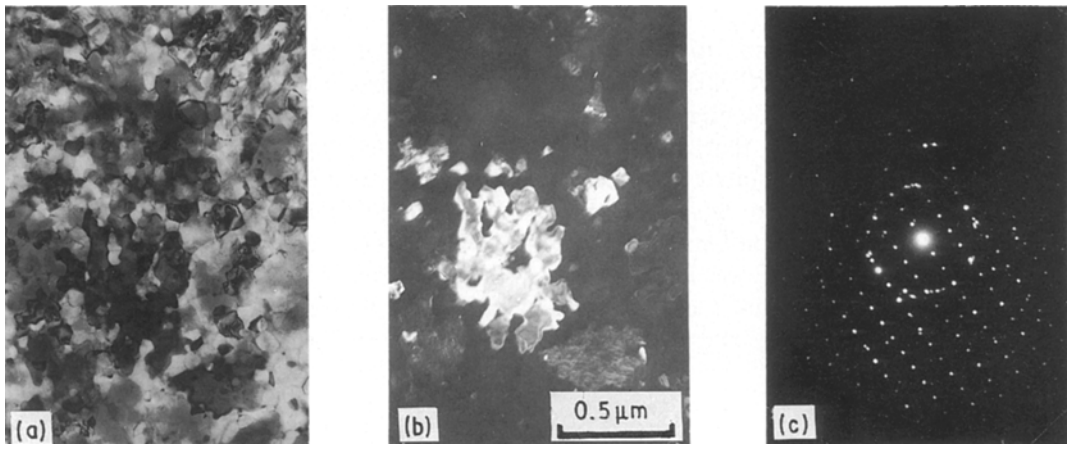

Figure 5 The t-Fe_3B crystallized from the amorphous phase in annealed vacuum-quenched ribbons: (a) bright-field micrograph; (b) dark-field micrograph; (c) SAD pattern of t-Fe_3B.

amount of precipitates was formed in the form of a network and divided the original cells into many subcells of smaller diameter, about 0.1 μm. These subcells existed until the annealing temperature reached 700 °C. The precipitates gave ring SAD patterns and their *d* values were in agreement with those of Fe_2B. In the samples annealed at or above 800 °C, the subcell morphology disappeared, but a great amount of granular precipitates was formed. Among them, one kind of precipitate was found by SAD to be Cr_2B; it was very easy to distinguish from other kinds of precipitate because it contained stacking faults. This phase had a higher growth rate. Its grain size normally was over 1 μm after annealing at 1000 °C; it was surrounded by α-Fe grains of similar size. SAD analysis indicated that another kind of precipitate was M_3B_2, which had a lower growth rate and retained a grain size of about 0.3 μm even after annealing at 1000 °C. Most of M_3B_2 grains were sited on the boundary of matrix α-Fe grains. In agreement with the above structural phenomena, the ribbons annealed below or at 700 °C were very brittle, but a certain ductility could be achieved by annealing at or above 800 °C. The ribbons annealed at 1000 °C could even be bent to 180° without fracture.

During annealing, the amorphous structure of the ribbons quenched in vacuum crystallized in two stages: α-Fe crystallized first, then a kind of boride formed (there were two crystallization peaks in the DTA curve: $T_{p1} = 508$ °C, $T_{p2} = 569$ °C, heating rate 20 °C min^{-1}). XRD and SAD analysis showed that this boride was body-centred tetragonal-Fe_3B (t-Fe_3B), different from the o-Fe_3B formed in melt-quenching. TEM illustrated (Fig. 5) that this boride grew independently during crystallization and exhibited irregular shapes due to the impediment of the fine precrystallized α-Fe grains. In the present alloys, t-Fe_3B was much more stable than o-Fe_3B. It still existed after annealing at 700 °C. Above 800 °C, there was no apparent difference in structure and constituent phases between the ribbons quenched in air and the ribbons quenched in vacuum.

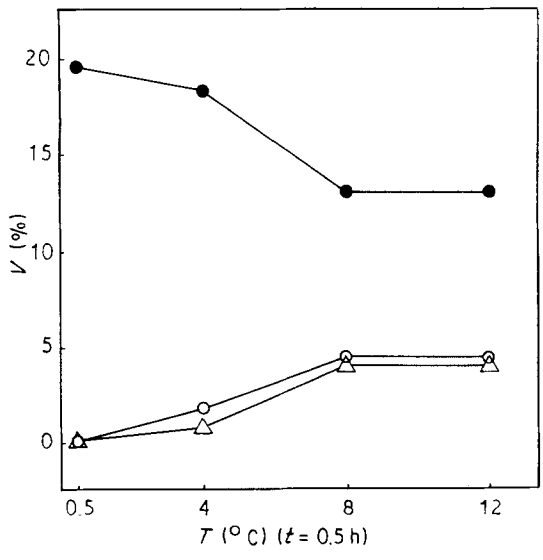

Figure 6 The boride volume fraction versus annealing time. (○) M_3B, (△) Cr_2B, (●) Fe_2B.

3.2.2. Transformation of borides during isothermal annealing

The precipitation process of borides at 700 °C is shown in Fig. 6. Only Fe_2B was found when the ribbons were annealed for 0.5 h and transformation into M_3B_2 and Cr_2B took place as the annealing time was prolonged. This process was controlled by the diffusion of Cr, Mo atoms. These borides eventually reached an equilibrium in quantity after annealing for 8 h and Fe_2B remained dominant. A similar process happened in ribbons annealed at 800 °C for different times, but less Fe_2B was found in eventual equilibrium. At temperatures higher than 800 °C, no Fe_2B was found by XRD except for during the initial stage of annealing. TEM results of the 700 °C/12 h annealed samples revealed much evidence of *in situ* transformation of Fe_2B to Cr_2B without individual nucleation of Cr_2B. As shown in dark-field images (Fig. 7), the Cr_2B with characteristic planar-fault fringes appears on the site of the original Fe_2B network.

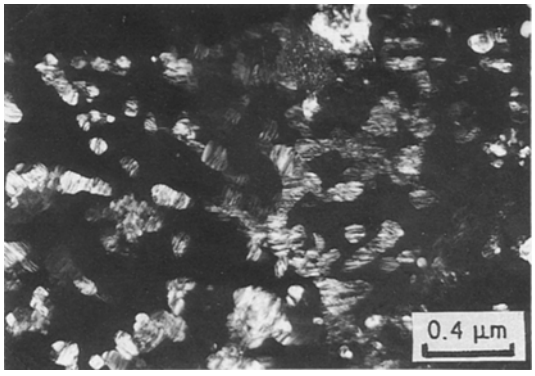

Figure 7 TEM dark-field micrograph of M_2B in 700 °C/12 h annealed samples.

3.2.3. The relation between Cr_2B and Fe_2B

In the high-temperature range, Cr_2B is more stable than Fe_2B (the melting point of Cr_2B is 1873 °C, and that of Fe_2B is only 1391 °C). Therefore, with increasing temperature, more and more Cr atoms will diffuse from the matrix into the borides to substitute for Fe. It has been pointed out that the solubility of Cr in Fe_2B is only 16 at % while that of Fe in Cr_2B is much higher [7]. At lower temperatures, M_2B may exist in the form of Fe_2B because of a lower Cr concentration (less than 16 at %) in M_2B. It will then turn into an equilibrium coexistence of Fe_2B and Cr_2B as a result of higher Cr concentration in excess of the solubility of Cr in Fe_2B at higher temperatures. In this way, as the temperature is raised, the Fe_2B-dominated M_2B will be gradually replaced by Cr_2B via an equilibrium coexistence between Fe_2B and Cr_2B.

Depending on the degree of similarity between their structures, the transformation from Fe_2B to Cr_2B may occur simply through atom substitution and structural adjustment. By comparing their lattice parameter, it can be found that $c_{Cr_2B} \simeq c_{Fe_2B}$, $b_{Cr_2B} \simeq 2^{1/2} b_{Fe_2B}$, $a_{Cr_2B} \simeq 2b_{Cr_2B}$. Therefore, in a single Cr_2B cell, just four Fe_2B units can be accommodated. On further examining the atomic arrangement [5, 8], we found that Cr_2B virtually consists of four sections: A, B, C, D, aligned along the *a*-axis, while the Fe_2B cell can be regarded as a combination of sections A and C (only a slight adjustment of boron atoms is needed) (Fig. 8). Therefore, the crystal structure of Fe_2B can be taken as a kind of stacking fault of Cr_2B and it can be reasonably deduced that the remaining Fe_2B may coexist with Cr_2B in the form of stacking faults as thin slices sandwiched between (1 0 0) faces of Cr_2B in order to lower their interfacial energy.

Fig. 9 shows a transmission electron micrograph of the stacking fault (the contrast of fringes is symmetrical in the bright-field image but asymmetrical in the dark-field image). And indeed, by trace analysis, the stacking fault plane was found to be (1 0 0). In agreement with the gradual decrease of the equilibrium Fe_2B quantity with annealing at increasing temperatures, the density of this fault was observed to be very large in the 700 °C/12 h annealed sample and to become progressively smaller with increasing temperature.

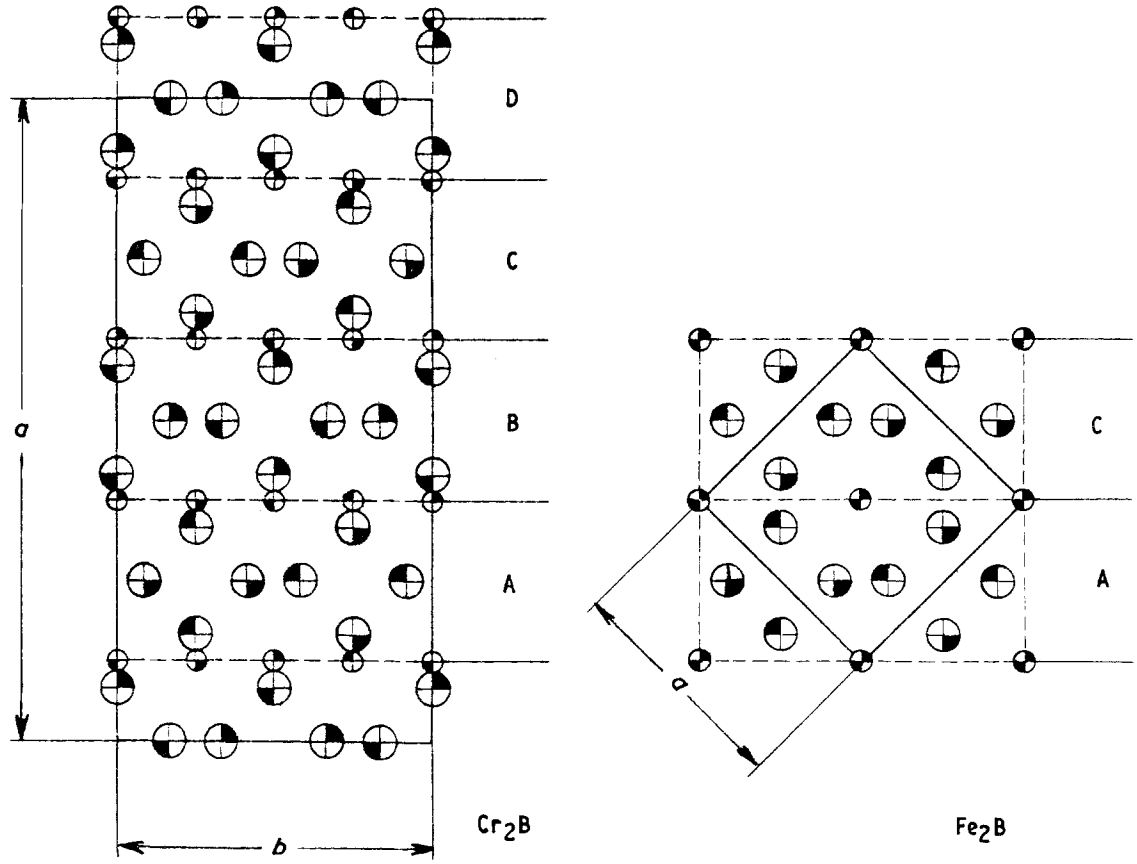

Figure 8 A comparison between crystal structures of Fe_2B and Cr_2B. (Counter clockwise change of the shaded quarter in the circle represents a displacement of *c*/4 in the *c*-axis direction). (○) Metal atom, (o) B atom.

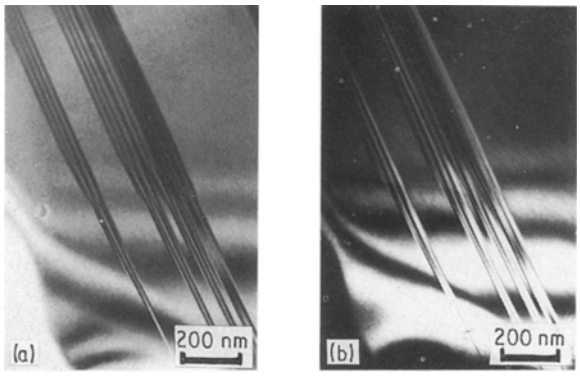

Figure 9 Transmission electron micrographs of the stacking faults in Cr_2B: (a) bright-field image; (b) dark-field image.

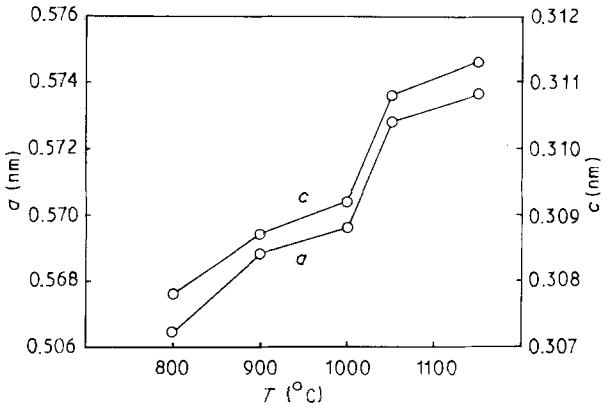

Figure 10 The lattice constants of M_3B_2 versus the annealing temperature.

3.2.4. The change in the lattice parameters of M_3B_2

The XRD diffraction lines of M_3B_2 moved continuously in the direction of higher d (interplanar spacing) values with increasing temperature. But during isothermal annealing, the prolonged annealing time did not result in any displacement of M_3B_2 lines. The change in the a and c values of the lattice parameter of M_3B_2 with annealing temperature is illustrated in Fig. 10. When their values changed, the ratio of c/a remained at nearly the same value of 0.543. It is generally accepted that M_3B_2 may have the form of MM'_2B_2 with a smaller lattice cell or the form of $M_2M'B_2$ with a larger lattice cell, where, M represents the metal atoms of larger radii (e.g. Mo) and M′ the metal atoms of smaller radii (e.g. Fe, Cr). The former can transform into the latter in a certain annealing temperature range [9]. The present results show that M_3B_2 may have a composition between MM'_2B_2 and $M_2M'B_2$. The Mo concentration in M_3B_2 will increase continuously with increasing temperature and there is a definite relation between the Mo concentration and annealing temperature. In addition, owing to the increment of both the concentration of Mo in M_3B_2 and the solubility of Mo in the α-Fe matrix, the amount of M_3B_2 showed a gradual decrease when the annealing temperature was raised above 950 °C [10].

3.2.5. The formation of $M_{23}B_6$

Except for those of Cr_2B and M_3B_2, new diffraction lines which were in accordance with the lines of $M_{23}(B, C)_6$ in boron-alloyed steels were seen in the XRD spectrum of 950 °C/2 h annealed samples; meanwhile the amounts of Cr_2B and M_3B_2 decreased. According to the composition of this alloy, the new phase should be $M_{23}B_6$; TEM and SAD analyses confirmed the existence of this phase (Fig. 11). In the present work, $M_{23}B_6$ only existed as a stable phase within a narrow temperature range. When the 950 °C/2 h annealed samples were re-annealed, the amount of pre-formed $M_{23}B_6$ decreased noticeably at 1050 °C and disappeared at 1150 °C, meanwhile the amount of Cr_2B and M_3B_2 increased again [10].

TEM observation illustrated that $M_{23}B_6$ had a very small nucleation rate but a high growth rate. The

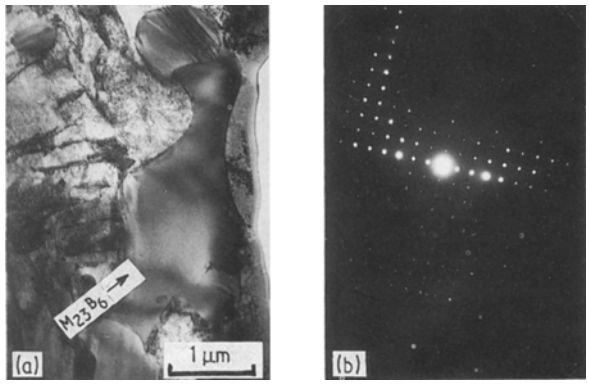

Figure 11 Transmission electron micrograph and SAD pattern of $M_{23}B_6$ in 950 °C/2 h annealed sample.

formation of $M_{23}B_6$ could be greatly accelerated by introduction of favourable nucleation sites such as dislocations. No $M_{23}B_6$ was found in the 950 °C/0.5 h annealed samples, but after these samples were annealed again, much more $M_{23}B_6$ was found in the 950 °C/0.5 h + 950 °C/1.5 h annealed samples than in the 950 °C/2 h annealed samples, due to the large number of dislocations induced near the Cr_2B/α-Fe interfaces by thermal stress during the cooling period after the first 950 °C/0.5 h annealing. The above results show that the transformation of Cr_2B and M_3B_2 to $M_{23}B_6$ is controlled by the nucleation of $M_{23}B_6$.

The DTA analysis on the 950 °C/0.5 h annealed sample indicated that the precipitation peak temperature of $M_{23}B_6$ was about 925 °C.

3.2.6. The composition of borides

Table I lists the results of STEMEDS and EPM analyses on borides and matrix.

A quantitative test for boron cannot be carried out by EDS, therefore the atomic percentage of boron was determined using stoichiometric calculation, assuming that Si atoms occupied the B atom positions in the crystal cell. The accurate composition of M_3B_2 could not be determined owing to the smallness of its grain size and oscillation of the electron beam during the experiment, but the test data indicated that M_3B_2 was

TABLE I Results of STEMEDS analyses (at %)

	Fe	Cr	Mo	Si	B
$M_{23}B_6$	53	24	2.3	0.8	(20)
$(Cr, Fe)_2B$	35	30	1.2	0.3	(33)
	33	36	1.0	0.2	30
Matrix	82	13	0.5	4	(0)
Original comp.	70	18	2	1	9

Note: Figures in brackets are obtained by calculation. Figures on lower lines for $(Cr, Fe)_2B$ are electron probe data.

rich in Mo and contained Cr and Fe. Repeated experiments on the composition of many Cr_2B grains gave similar results which were close to FeCrB. On further comparing the matrix composition with the original alloy composition, it was found that the combining tendencies of the elements with B decreases in the sequence Mo > Cr > Fe > Si, similar to those with carbon in steels.

3.2.7. The influence of boron concentration on borides

XRD analysis showed that under similar single-roller processing conditions, after 950 °C/0.5 h annealing, the change in B concentration did not result in an alteration of existing boride forms, they were still Cr_2B and M_3B_2. However, the amount of borides changed with different B percentage. The amount of Cr_2B increased in approximately linear relation with the increase in B atomic percentage in the alloy, but the amount of M_3B_2 was almost unchanged (Fig. 12). If we extrapolate this relation to the point where the amount of Cr_2B reaches zero, a B concentration of 1.8 at % remains, which apparently belongs to M_3B_2. (Note: based on this, we calculated, using the crystal cell parameters of borides, $V_{M_3B_2} = 4\%$, $V_{Cr_2B} = 18\%$ when B concentration was 9%. Then, by comparing the integrated intensity of XRD lines, we obtained other data for volume fraction shown in Fig. 12 and also those in Figs 3 and 6). When the Mo atom percentage was raised from 2% to 6% under conditions where the B concentration remained at 9 at %, the amount of M_3B_2 became four times as much as that in the original alloy, and correspondingly, the amount of Cr_2B decreased by 80%. The above results indicate that in the distribution of boron between Cr_2B and M_3B_2, B has a preference for the formation of M_3B_2, which may be related to the stronger combining tendency of Mo with B. As long as sufficient B is added, the quantity of M_3B_2 is determined only by the Mo concentration in the alloy. TEM observation showed that, with increasing B percentage, the homogeneously dispersed boride particles grew to come into contact with each other [4]. Eventually, when the B atomic percentage reached 20%, the borides formed a continuous frame with α-Fe grains embedded in it. Correspondingly, the ductility of the ribbons decreased with the increasing B percentage. The ribbons could be bent to 180° without fracture when the B concentration was below 10.5 at % but were extremely brittle when it was 20 at %.

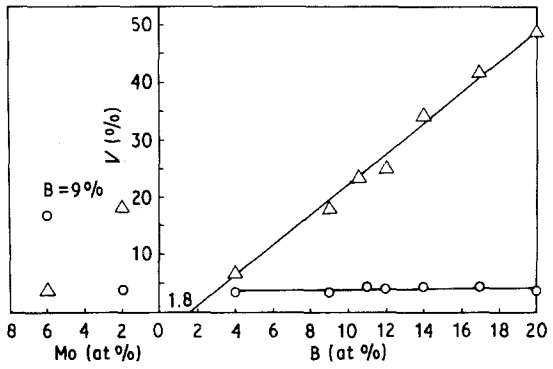

Figure 12 The volume fraction of borides versus the boron concentration. (△) Cr_2B, (○) M_3B_2.

TABLE II Structure unit cell parameters of borides

Boride	Crystal system	Lattice constants (nm)
o-M_3B	ortho.	$a = 0.543$, $b = 0.445$, $c = 0.666$
t-M_3B	bct.	$a = 0.865$, $c = 0.429$
$(Fe, Cr)_2B$	bct.	$a = 0.510$, $c = 0.424$
$(Cr, Fe)_2B$	fc ortho.	$a = 1.457$, $b = 0.732$, $c = 0.422$
M_3B_2	tetra.	$a = 0.566$–0.574, $c = 0.308$–0.311
$M_{23}B_6$	fcc	$a = 1.062$

4. Conclusion

Four kinds of borides form in the as-melt-quenched and annealed Fe-Cr-Mo-B-Si alloys. They are M_3B, M_2B, M_3B_2 and $M_{23}B_6$. Their crystal unit cell parameters are summarized in Table II.

1. M_3B: there are two forms of M_3B, based either on o-Fe_3B (isomorphous with Fe_3C) or on t-Fe_3B (isomorphous with Fe_3B). The o-Fe_3B nucleates and grows during the rapid solidification of the ribbons, and presents in the form of α-Fe + o-Fe_3B eutectic. It disappears upon annealing at temperatures above 300 °C. The t-Fe_3B forms during the annealing crystallization of the amorphous ribbons; it is more stable than o-Fe_3B and still remains even after annealing at 700 °C for 0.5 h.

2. M_2B: M_2B also exists in two forms, based either on Fe_2B (isomorphous with $CuAl_2$) or on Cr_2B (isomorphous with Mn_4B). Fe_2B precipitates in a network morphology from the supersaturated α-Fe solid solution at the initial stage of annealing. At higher temperatures, it transforms into granular Cr_2B and M_3B_2. As the temperature is raised, M_2B gradually transforms from an Fe_2B-dominated state to a Cr_2B-dominated state via the equilibrium coexistence between Fe_2B and Cr_2B. The actual composition of Cr_2B is close to FeCrB. Cr_2B may be formed by transformation of Fe_2B through atomic substitution and structural adjustment. The remaining Fe_2B may be sandwiched in the form of thin slices between (1 0 0) faces of Cr_2B as stacking faults.

If the alloy composition is close to M_4B, a new metastable phase which has a crystal structure similar to that of Cr_2B but virtually being a hexagonal lattice will form upon rapid solidification.

3. M_3B_2: its composition can be expressed as $Mo_{1+x}(Fe, Cr)_{2-x}B_2$. x increases continuously from 0–1 with increasing temperature and has a definite relation with temperature. In the distribution of B between M_2B and M_3B_2, B has a preference for the formation of M_3B_2. Hence under the conditions of sufficient B being added, the quantity of M_3B_2 depends on the Mo concentration in the alloy. The amount of M_3B_2 reaches the highest value between 800 and 900 °C and decreases at higher temperatures owing to the increase in both the Mo concentration in M_3B_2 and the Mo solubility in α-Fe.

4. $M_{23}B_6$: in a narrow temperature range around 925 °C, with increasing annealing time, the pre-formed M_2B and M_3B_2 further transform into $M_{23}B_6$. This transformation is controlled by the nucleation of $M_{23}B_6$.

Acknowledgements

The authors thank Mr You Yonlong, Mr Jing Chunyong, Mr Zhang Xiaomin, Mr Yan Shouping and Ms Yu Quanqin for their technical assistance, and Dr Xu Jialong and Dr Zhang Jingguo for their permanent support and helpful advice. The authors also thank Professor R. W. Cahn for reviewing the manuscript.

References

1. R. RAY, V. PANCHANATHAN and S. ISSEROW, *J. Metals* **35**(6) (1983) 30.
2. W. E. BROWER, R. STRACHAN Jr and M. C. FLEMINGS, *Cast Met. Res. J.* **6** (1970) 176.
3. LIN YIJIAN, YOU YUNLONG, ZHANG XIAOMIN, JING CHUNYONG and YU QUANQIN, *Acta Metall. Sin. (English Edn) B* **2** (1989) 177.
4. LIN YIJIAN, YOU YUNLONG, JING CHUNYONG and YU QUANQIN, *J. Iron Steel Res.* **2**(2) (1990) 55 (in Chinese).
5. B. E. BROWN and D. J. BEERNTSEN, *Acta Crystallogr.* **17** (1964) 448.
6. A. GARCIA and W. KESTERNICH, *Scripta Metall.* **19** (1985) 57.
7. G. PRADELLI and C. GIANOGLIO, *Metall. Ital.* **68** (1976) 591.
8. ROLAND KIESSLING, *Acta Chem. Scand.* **4** (1950) 146.
9. R. T. HOLT and W. WALLACE, *Int. Metall. Rev.* **21** (1976) 1.
10. LIN YIJIAN, HU JIAN, YOU YUNLONG, JIN CHUNYONG and YU QUANQING, *Acta Metall. Sin. (English Edn) B* **3** (1990) 185.

Received 6 August
and accepted 17 August 1990